Computational investigation of half-Heusler/MgO magnetic tunnel junctions with (001) orientation

Jianhua Ma, Yunkun Xie, Kamaram Munira, Avik W. Ghosh, and William H. Butler

View Online **Export Citation** **CrossMark**

Computational investigation of half-Heusler/MgO magnetic tunnel junctions with (001) orientation
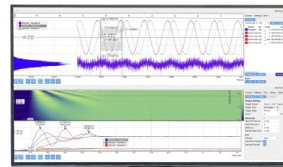
Jianhua Ma,[1,a)] Yunkun Xie,[1] Kamaram Munira,[2] Avik W. Ghosh,[1,3,b)] and William H. Butler[2,4,c)]

AFFILIATIONS

[1]Department of Electrical and Computer Engineering, University of Virginia, Charlottesville, Virginia 22904, USA
[2]Center for Materials for Information Technology, University of Alabama, Tuscaloosa, Alabama 35401, USA
[3]Department of Physics, University of Virginia, Charlottesville, Virginia 22904, USA
[4]Department of Physics and Astronomy, University of Alabama, Tuscaloosa, Alabama 35401, USA

[a)]Author to whom correspondence should be addressed: jm9yq@virginia.edu
[b)]Electronic mail: ag7rq@virginia.edu
[c)]Electronic mail: wbutler@mint.ua.edu

ABSTRACT

A series of half-metallic XYZ half-Heusler alloys is combined with MgO to create Heusler–MgO junctions. The electronic and magnetic properties of these junctions are investigated. The strong oxidation between metal and oxygen atoms causes the systems with pure YY interfaces to be the most stable cases. We conclude that uniaxial anisotropy can be induced in Heusler layers adjacent to MgO. The type of interface layers determines the half-metallicity and anisotropy (in-plane or perpendicular) in the Heusler–MgO junctions. The capacity to retain both half-metallicity and perpendicular magnetic anisotropy in NiMnSb/MgO and CoTiSn/MgO junctions with a MnMn interface layer makes these structures potential candidates as electrode layers in spin transfer torque random access memory devices.

Published under an exclusive license by AIP Publishing. https://doi.org/10.1063/5.0051816

I. INTRODUCTION

Spin transfer torque random access memory (STT-RAM) has attracted a great deal of attention and has now been commercialized based on its potential to combine the speed of static RAM (SRAM), the density of dynamic RAM (DRAM), and the nonvolatility of flash while providing excellent scalability and outstanding endurance.[1] The magnetic tunneling junction (MTJ) inside an STT-RAM cell stores information in the relative magnetic orientations of the electrode layers, with STT switching resulting in magnetization reversal of a softer free layer. In order to fabricate a practical STT-RAM, a robust magnetic tunnel junction (MTJ) with optimized and matched interfaces between barriers and electrodes is necessary.[2] This requires a magnetic material with high spin polarization, low saturation magnetization, low magnetic damping, and perpendicular magnetic anisotropy (PMA).[3] If the materials are compatible with MgO at crystal interfaces, that would make them particularly promising for spintronic applications due to the known ability of MgO to symmetry filter the various tunneling bands.

Half-metals (HMs) have been widely studied as one of the most promising electrode materials in the field of spintronics. These materials have a gap at the Fermi level in one spin channel for the bulk while showing metallic behavior in another spin channel. The resultant highly spin-polarized current is critical to a low energy read–write current drive. The first half-metal, the half-Heusler alloy NiMnSb, was recognized in a calculation by de Groot and collaborators in 1983.[4] Since then, a series of half-metal and near-half-metal Heusler alloys has been identified theoretically.[5–10] In order to do a systematic search within the Heusler alloy family, we created a Heusler alloy database including electronic structures, magnetism, and structure stability studies of 378 half-Heusler alloys.[11] From the half-Heusler database, we have identified 45 half-metals and 34 near-half-metals with negative formation energy that follow the Slater–Pauling rule of three electrons per atom. Unfortunately, most of the above half-metals and near-half-metals do not have compatible lattice constants with MgO. Furthermore, their $C1_b$ cubic symmetry prevents any uniaxial magnetocrystalline anisotropy (MCA) needed for data retention as a magnetic layer.

In this paper, we identify six half-metals and near-half-metals with less than 1% lattice mismatch with MgO, and we calculate first principles electronic bands of their heterostructures. Section II describes the supercell structures simulated, while Sec. III presents the electronic structure results of various Heusler–MgO systems. We show that a large ($> 10^5$) ballistic tunnel magnetoresistance (TMR) is possible in these systems as the half-metallicity persists with MgO.

II. STRUCTURE AND COMPUTATIONAL METHOD

Calculations were performed for periodic Heusler–MgO junction superlattices consisting of five layers of MgO (B1 unit cell, lattice constant $a = 5.95$ Å) and five layers of the half-Heusler alloys using density-functional theory (DFT) as implemented in the Vienna *Ab initio* Simulation Package (VASP)[12] and using a plane wave basis set and the projector augmented wave (PAW) method.[13] A uniform cut-off energy of 520 eV was implemented for all calculations. The Perdew–Burke–Ernzerhof (PBE) version of the generalized gradient approximation (GGA) to the exchange-correlation functional of DFT was adopted.[14] In order to take into account all degrees of freedom for the Heusler–MgO interfaces, we performed full structural optimizations for the superlattice parameters and internal coordinates. The convergence criterion of the change in total energy was set to 10^{-5} eV. We took a $12 \times 12 \times 2$ k-point mesh for the (100) transverse interface between the alloy and MgO.

The half-Heusler alloy of the form XYZ crystallizes in the face-centered cubic C1$_b$ structure ($F\bar{4}3$ m) with one formula unit per unit cell. It consists of four sublattices: X at the $(\frac{1}{4}, \frac{1}{4}, \frac{1}{4})$, Y at the $(\frac{1}{2}, \frac{1}{2}, \frac{1}{2})$, Z at the $(0,0,0)$, and the vacancies at the $(\frac{3}{4}, \frac{3}{4}, \frac{3}{4})$ sites. The six half-Heusler alloys we studied here are CrScAs, MnVSb, FeTiSb, CoTiSn, NiTiIn, and NiMnSb. To the best of our knowledge, none of these have been synthesized except for NiMnSb.[15] The calculated lattice constant of NiMnSb (5.91 Å) is within 1% of the experimental result (5.92 Å).[15] The [100] direction of these alloys and the [110] direction of MgO present a nearly perfect lattice match.

We studied four Heusler terminations as presented in Fig. 1: (a) X (three layers of X and two layers of YZ in total across the Heusler slab), (b) XX (two layers of XX, one layer of X, and two layers of YZ in total), (c) YZ (two layers of X and three layers of YZ in total), and (d) YY (two layers of YY, one layer of YZ, and two layers of X in total) terminals. The XX termination means that the vacancies in the bulk are occupied by X atoms at the interfaces, but the X layers inside the bulk still retain their vacancies. The YY terminations mean that the Z atoms in the YZ termination are replaced by Y atoms. More structural details are discussed in Sec. III.

III. RESULTS AND DISCUSSION

We performed full ionic relaxations for the six Heusler/MgO supercells to obtain their equilibrium structures. There are four terminations for each Heusler/MgO supercell as shown in Fig. 1. The bond types and lengths at the different interfaces are listed in Table I. For example, the Cr/OMg interface is composed of a layer containing only Cr atoms and a layer containing both O and Mg atoms with direct Cr–O bonds. We notice that the bond length is the shortest at the X/OMg-terminated interfaces in all six
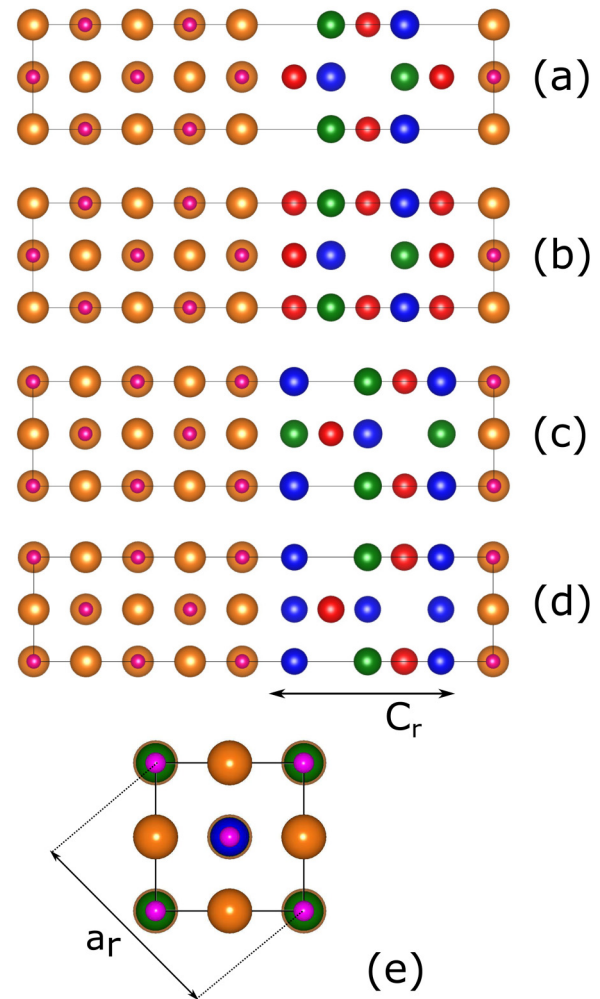

FIG. 1. Side views of the superlattices of the half-Heusler(110)/MgO junctions: (a) X/OMg-terminated interface, (b) XX/OMg-terminated interface, (c) YZ/OMg-terminated interface, and (d) YY/OMg-terminated interface. Color note: X (red), Y (blue), Z (green), Mg (orange), and O (pink).

Heusler–MgO junctions, while the optimized Y/Z–O bonds are typically the longest at the YZ/OMg interfaces. We suppose that the longer bond results from the bigger atomic size of Ti, Sc, Sb, and Sn.

We also analyzed the bonding strength of the interfaces by calculating their binding energies W. W is the binding energy of the two interfaces on both sides of the Heusler layer,

$$W = E_{\text{XYZ/MgO}} - E_{\text{XYZ}} - E_{\text{MgO}}, \qquad (1)$$

where $E_{\text{XYZ/MgO}}$ is the total energy of the optimized Heusler–MgO junctions, while $E_{\text{XYZ}}(E_{\text{MgO}})$ is the total energy of the Heusler (MgO) slab surrounded by vacuum in a supercell. The lattice parameters of the slab supercells are taken to be the same as those

TABLE I. Bond lengths and binding energy W for the half-Heusler(100)/MgO interfaces.

Interface terminal	Bond type	Bond length (Å)	W (eV)
Cr	Cr–O	2.06	−2.69
CrCr	Cr–O	2.10	−3.83
ScAs	Sc–O/As–O	2.30/3.11	−1.74
ScSc	Sc–O	2.32	−3.74
Mn	Mn–O	2.03	−2.34
MnMn	Mn–O	2.13	−2.92
VSb	V–O/Sb–O	2.32/2.88	−1.51
VV	V–O	2.10	−4.26
Fe	Fe–O	1.98	−2.47
FeFe	Fe–O	2.05	−3.99
TiSb	Ti–O/Sb–O	2.34/2.92	−1.64
TiTi	Ti–O	2.18	−4.35
Co	Co–O	1.96	−2.47
CoCo	Co–O	2.02	−4.21
TiSn	Ti–O/Sn–O	2.29/2.74	−2.00
TiTi	Ti–O	2.18	−4.23
Ni	Ni–O	2.00	−2.05
NiNi	Ni–O	2.07	−3.21
TiIn	Ti–O/In–O	2.26/2.57	−2.39
TiTi	Ti–O	2.18	−4.35
Ni	Ni–O	2.01	−2.06
NiNi	Ni–O	2.08	−3.22
MnSb	Mn–O/Sb–O	2.46/3.01	−1.84
MnMn	Mn–O	2.18	−3.65

of the optimized Heusler–MgO junctions, and no further relaxation is performed for the slab supercells. We need to point out that relative stability of the interfaces of MTJs with Heusler electrodes could also be studied employing more elaborated *ab initio* atomistic thermodynamics.[16,17] These calculations can be considered in the future work.

We found that the YY/OMg interfaces present the lowest binding energies for most Heusler–MgO junctions except CrScAs–MgO. The mechanism behind the binding energies is complicated for different interface termination. First, the X-rich (XX) interface has more X–O bonds than the X interface with vacancies per unit cell; therefore, the X-rich interface has lower binding energy than the X interface. Second, the Y element is the most electropositive element in XYZ; therefore, we propose that the oxidation and bonding between Y–O atoms is stronger than X–O atoms. Previous investigation also predicted that full-Heusler alloys tend to stabilize in pure XX or YY layers[18] due to strong oxidation. Third, the bigger atomic size at the interface may increase the bond length. The size of Sc is the largest among the Y elements in this work; therefore, the bond length (2.32 Å) at the Sc-rich (ScSc) interface is larger than the Cr-rich (CrCr) interface (2.10 Å). The Cr-rich interface has lower binding energy than the Sc-rich interface.

Table II lists the geometric and magnetic properties of Heusler–MgO junctions. a_r is the lattice parameter obtained from the layer parallel with the interface after relaxation, while c_r is the average lattice parameter of the four "internal" spacings in five

Heusler layers. If the c_r/a_r value is larger than 1.01, we interpret that this Heusler layer has been distorted to a tetragonal structure. The in-plane lattice variation is calculated compared to the bulk lattice constants. The largest variation is 3.8% for the ScSc interface. The possible reason for a large variation for this case is that the bigger atomic size of Sc distorts the interface layer more seriously. However, most of the in-plane lattice variation is less than 1%. As the thickness of Heusler layers increases, the in-plane lattice variation and distortion will be reduced.

Table II also includes the saturation magnetization (M_S) and the induced anisotropy on one interface side ($\perp K$). The induced anisotropy is calculated by comparing the differences between ground state energies, whose magnetic moments are aligned along (001) and (100) directions. A positive anisotropy K suggests that the magnetization prefers to be perpendicular to the Heusler–MgO interfacial plane, while a negative one implies that the magnetization tends to lie in-plane. We also consider the competition between induced anisotropy and shape anisotropy because shape anisotropy in thin films usually dominates over magnetocrystalline anisotropy. We define the critical thickness t as the threshold value for induced anisotropy to overcome shape anisotropy when thickness is less than t. The t is introduced in a shape anisotropy equation,

$$E_{\text{induced}} = E_{\text{shape}} = \frac{1}{2} t \mu_0 M_S^2, \tag{2}$$

where E_{induced} and E_{shape} are the induced anisotropy energy and the shape anisotropy energy through the unit area in-plane on one interface side, respectively. The critical thickness is listed in Table II. If the thickness c_r of the Heusler layers is less than critical thickness t, the induced anisotropy can overcome the in-plane shape anisotropy.

Although the uniaxial anisotropy is induced by the tetragonal distortion in the Heusler layers, its value and easy axis direction are not determined by c_r/a_r. The value of uniaxial anisotropy is significantly conditioned by the atoms at the Heusler layer interface. For example, for TiSb interface layers at the FeTiSb/MgO junction, the anisotropy is in-plane, while Fe and FeFe interface layers generate significant perpendicular anisotropy. Also, if the interface layer thickness c_r is less than the corresponding critical thickness t, its induced perpendicular anisotropy dominates over the shape anisotropy.

The final column in Table II is whether the supercell still retains half-metallicity (HM) or near-half-metallicity (NHM). From the final column, it is obvious that locally modified stoichiometry at the interface changes the metallicity. For example, the VV interface is near-half-metallic for the MnVSb/MgO structure, while the VSb interface is metallic. We confirm that all the layers including the middle VSb layer in the VSb termination structure are metallic. Therefore, combination of the X- or Y-rich interface terminations may drastically change its physical properties at the center of the Heusler layer.

As discussed before, an ideal Heusler magnetic electrode needs to have not only enough PMA but also adequate half-metallicity of the Heusler layers. The latter attribute is very difficult to retain in supercells and is in fact governed by the interface type. Interestingly, we find that only systems with YY interface layers sometimes remain half-metallic or near-half-metallic, as seen in Figs. 2 and 3, while all other interfaces lose their half-metallicity.

TABLE II. Summary of the geometric and magnetic properties of various half-Heusler–MgO junctions. We list the calculated lattice constant in bulk a, interface type, relaxed lattice constants a_r and c_r, relaxed ratio between c_r/a_r, saturation magnetization M_S, induced anisotropy ($\perp K$), critical thickness t, and half-metallicity (bulk CrScAs is in the tetragonal phase and it has two lattice constants in the second column).

XYZ	a (Å) in bulk	Interface (Å)	Relaxed a_r, c_r (Å)	% change in a_r for Heusler	Relaxed c_r/a_r	M_S (emu/cm^3)	$\perp K \times 10^6$ (erg/cm^3)	Critical thickness, t (Å)	Half-metallic?
CrScAs (HM)	5.92, 6.54	ScAs	5.87, 6.86	−0.79	1.1684	618	−0.89		No
		Cr	5.92, 6.92	0.01	1.1693	896	−2.40		No
		CrCr	6.03, 6.23	0.19	1.0428	747	−0.31		No
		ScSc	6.15, 6.08	3.8	0.9889	475	0.79	7.25	No
MnVSb (HM)	5.92	VSb	5.90, 6.13	−0.27	1.0371	59	6.75	207.55	No
		Mn	5.96, 6.03	0.64	1.0116	372	−1.21		No
		MnMn	6.00, 6.08	1.30	1.0156	737	0.66	20.14	No
		VV	5.92, 5.52	0	0.9345	381	−1.18		NHM
FeTiSb (NHM)	5.95	TiSb	5.89, 5.93	−0.94	1.0063	72	−1.68		No
		Fe	5.92, 5.96	−0.44	1.0055	208	5.27	177.56	No
		FeFe	5.98, 5.87	0.45	0.9882	421	5.09	168.90	No
		TiTi	5.98, 5.64	0.55	0.9431	0	0		No
CoTiSn (NHM)	5.93	TiSn	5.91, 5.93	−0.30	1.0028	0	0		No
		Co	5.90, 5.93	−0.43	1.0049	14	1.19	38.44	No
		CoCo	5.96, 5.80	0.51	0.9805	0.90	−0.00017		No
		TiTi	5.98, 5.66	0.89	0.9461	160	1.28	39.64	NHM
NiTiIn (NHM)	5.99	TiIn	5.97, 5.88	−0.26	0.9846	70	0.238	7.53	No
		Ni	5.92, 6.09	−1.19	1.0295	0.01	0		No
		NiNi	5.94, 6.16	−0.85	1.0375	13	−1.79		No
		TiTi	6.00, 5.74	0.17	0.96	248	0.056	1.71	NHM
NiMnSb (HM)	5.91	MnSb	5.89, 5.76	−0.42	0.9802	1130	8.10	14.40	No
		Ni	5.93, 5.78	0.27	0.9757	811	0.018	0.03	No
		NiNi	5.96, 5.83	0.79	0.9791	796	−2.83		No
		MnMn	5.96, 5.56	0.79	0.9327	1881	2.15	3.68	HM

One might argue that the in-plane distortion of a_r also influences half-metallicity so that the MnVSb/MgO junction with the VV interface layer resembles the bulk system with near-half-metallicity, while other systems become metallic. However, in the case of NiMnSb, the amount of in-plane distortion is the same for both NiNi and MnMn interface layers, but the Heusler layer loses its half-metallicity only for the NiNi interface layer. It has been verified experimentally by spin-resolved x-ray photoemission spectroscopy (SR-XPS) of an NiMnSb/MgO(100) junction that an Mn interface layer can be achieved, and some oxidization of Mn exists when an MgO(001) epitaxial barrier is grown on top of NiMnSb using molecular beam epitaxy (MBE).[19,20] However, the half-metallicity and the high TMR ratio of the NiMnSb–MgO junction have not yet been observed in experiments due to a decrease of the Mn magnetization at the interface with MgO.[19,21] Much like anisotropy, the interface layer seems to play a dominant role in determining half-metallicity over in-plane distortion. We also point out that although induced PMA is predicted for an NiMnSb/MgO junction with a pure MnMn interface, the large saturation magnetization M_S of NiMnSb will force the magnetization to lie in-plane because

its thickness c_r (5.56 Å) is very close to its corresponding critical thickness t (3.68 Å). This is in fact the same as other near-half-metallic Heusler–MgO junctions except CoTiSn.

IV. BALLISTIC I–V CHARACTERISTICS OF HALF-HEUSLER–MgO MTJs

While the tunnel magnetoresistance (TMR) of the superlattice will depend on defect states, spin depolarization, and incoherent scattering at room temperature, such effects tend to be geometry specific and hard to predict. Accordingly, a computational measure of the impact of half-metallicity is the ballistic current, which would at the least include the impact of a finite bias and the various effective masses across the tunnel junction. The transport calculations are performed in SMEAGOL,[22] which employs the nonequilibrium Green's function (NEGF) method combined with density-functional theory (DFT) in the SIESTA package[23] on a pseudo-atomic orbital basis set.[24] Double-ζ[25–27] is used for all orbitals, and the generalized gradient approximation (GGA) with Perdew–Burke–Ernzerhof (PBE) functional is adopted throughout
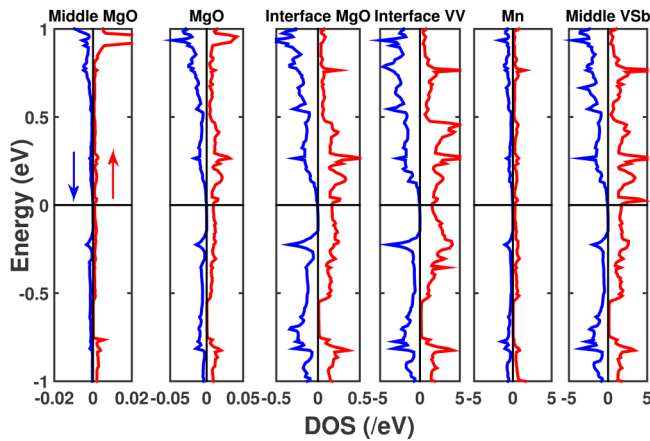
FIG. 2. Local density of states (DOS) for an MnVSb–MgO periodic supercell with a VV/OMg interface. The supercell stays NHM (the bandgap is opened in the spin-down channel). The maximum valence band edge is -0.1549 eV, and the minimum conduction band edge is -0.0349 eV. The bandgap is 0.12 eV. The bandgaps in all the layers are the same.

all calculations. The electronic temperature is set at 300 K. The spin-dependent current ($\sigma = \uparrow, \downarrow$) is calculated from

$$I^\sigma(V) = \frac{e}{h} \int T^\sigma(E; V)(f_L - f_R)dE, \quad (3)$$

$$T^\sigma(E; V) = \text{Tr}\left[\Gamma_L^\sigma G^\sigma \Gamma_R^\sigma G^{\sigma\dagger}\right], \quad (4)$$

where $T^\sigma(E; V)$ is the bias-dependent transmission and $f_{L,R}$ are the Fermi–Dirac distribution for the left/right Heusler contact, respectively. The transmission is calculated using NEGF,[28,29] where G^σ is
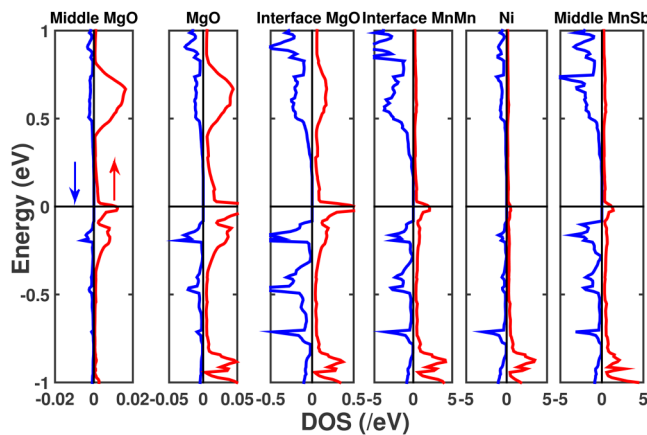

FIG. 3. Local density of states for a NiMnSb–MgO periodic supercell with an MnMn/OMg interface. The supercell stays HM (the bandgap is opened in the spin-down channel). The maximum valence band edge is -0.0927 eV, and the minimum conduction band edge is 0.1773 eV. The bandgap is 0.27 eV. The bandgaps in all the layers are the same.

the retarded Green's function and $\Gamma_{L,R}^\sigma$ are energy-dependent broadening matrices obtained from the anti-Hermitian parts of the recursively computed[22] left/right contact self-energies. At equilibrium, a $5 \times 5\mathbf{k}_\perp$-point mesh is used to converge the charge density, and then a $20 \times 20\mathbf{k}_\perp$-point mesh is used to calculate the spin-dependent current. At a finite bias, a constant potential is added to the Heusler contacts and a linear Laplace potential is added in the MgO. This approximation has been verified to be appropriate for magnetic tunnel junctions where the voltage drops mostly in the high resistant MgO.[30] Such an approximation considerably reduces the computational cost for self-consistent calculations in SMEAGOL.

Figure 4 shows the ballistic I–V characteristics of the six MTJs. Among them, NiMnSb shows higher current density ($\sim 10^8$ A/cm^2) than the other ($\sim 10^5$ A/cm^2). The reason for the big difference in current amplitude is because for NiMnSb, the Fermi energy in the conducting spin channel lies in the middle of the s band, which has the lowest decay rate inside MgO due to the same orbital symmetry as the Δ_1 band in MgO. Other systems are symmetry filtered as their conducting spin channel Fermi energies lie in the non-Δ_1 symmetry bands,[31] potentially due to the different work functions of the electrode materials. Therefore, the energy barrier heights between MgO and the electrodes are different, resulting in different tunneling probabilities.

MTJs are widely used in read units where the tunnel magnetoresistance (TMR) ratio is a key metric. The TMR can be calculated from the currents in parallel and anti-parallel configuration,

$$\text{TMR} = \frac{I_p - I_{ap}}{I_{ap}}. \quad (5)$$

Figure 5 shows the TMR ratio as a function of the voltage for the six MTJs. Out of the six junctions, four of them show high TMR at a low bias. It is worth mentioning that the specific value of the TMR ratio for a single junction is not important because our current calculations assume full ballistic transport without any
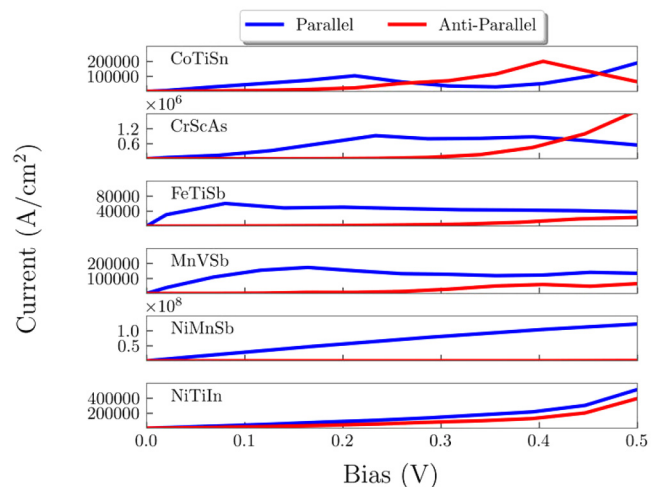

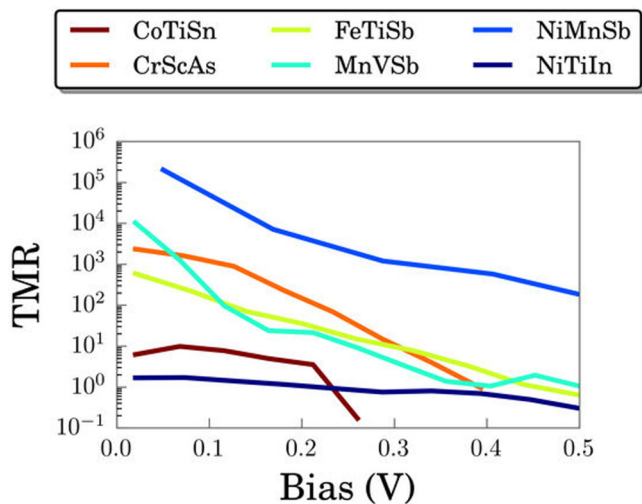**FIG. 4.** I–Vs of the half-Heusler/MgO/half-Heusler junction.

FIG. 5. The tunnel magnetoresistance of half-Heusler/MgO magnetic tunnel junctions.

spin scattering mechanism. Since the denominator I_{ap} is a very small number, any spin scattering can alter the TMR greatly. Depending on the specific mechanism, the TMR can vary with temperature[32] or magnetic impurity concentration. Still, comparing the
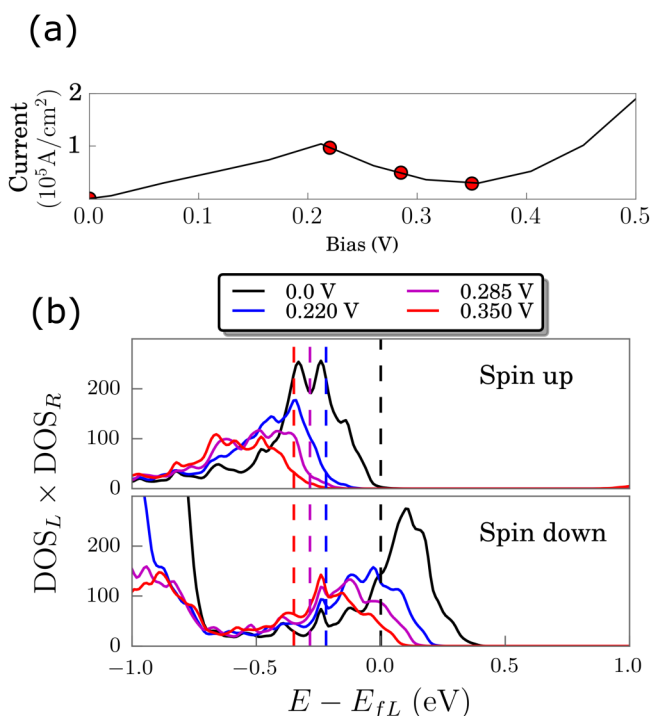

FIG. 6. (a) *I–V* of CoTiSn/MgO/CoTiSn in a parallel configuration. (b) The product of the DOS from left and right electrodes at a finite bias.

ballistic TMRs across different junctions provides a convenient reference point for which electrode materials might be better suited to low energy read operation in MgO-based MTJs.

Some of the systems show a negative differential resistance (NDR) at a moderate bias. Such an NDR is not hard to see in idealized geometries with sharp features in their density of states (e.g., Fig. 9 in Ref. 33). We use CoTiSn to illustrate the underlying mechanism. NDR here arises due to a competition between an ever-expanding Fermi window under a bias vs the progressive alignment then misalignment between sharp peaks in the contact densities of states sweeping past each other. The increasing Fermi window dominates the increase of current at a low bias, between 0 and 0.22 V. After that, the transmission starts to shrink with growing misalignment between contact densities of states away from zero bias. In the bottom plot of Fig. 6, we clearly see that within 0.22–0.35 V, the product of the contact DOS in the bias window keeps dropping for both spin channels. The competing effects lead to the observed NDR in the I–V. In reality, the NDR is probably hard to observe as the sharp DOS features get washed out by non-idealities, defects, and imperfections.

V. CONCLUSION AND FUTURE WORK

In this paper, we establish that it is possible to obtain uniaxial perpendicular magnetic anisotropy (PMA) and to retain half-metallicity (HM) in a Heusler–MgO junction, leading to an enormous ballistic finite temperature TMR between 10^3 and 10^5 at a low bias. Our results motivate further search and discovery of half-Heusler alloys as potential electrode materials in STT-RAM devices. Further theoretical works including chemical and group theoretical analyses are needed to explain the observed relation between the interface layer vs PMA and HM.

ACKNOWLEDGMENTS

DATA AVAILABILITY

The data that support the findings of this study are available from the corresponding author upon reasonable request.

REFERENCES

[1]J.-G. Zhu, Proc. IEEE **96**, 1786 (2008).
[2]K. Munira, W. H. Butler, and A. W. Ghosh, IEEE Trans. Electron Dev. **59**, 2221 (2012).
[3]E. Chen, D. Apalkov, Z. Diao, A. Driskill-Smith, D. Druist, D. Lottis, V. Nikitin, X. Tang, S. Watts, S. Wang, S. Wolf, A. Ghosh, J. Lu, S. Poon,

M. Stan, W. Butler, S. Gupta, C. Mewes, T. Mewes, and P. Visscher, IEEE Trans. Magn. **46**, 1873 (2010).

[4] R. A. de Groot, F. M. Mueller, P. G. v. Engen, and K. H. J. Buschow, Phys. Rev. Lett. **50**, 2024 (1983).

[5] I. Galanakis, P. H. Dederichs, and N. Papanikolaou, Phys. Rev. B **66**, 134428 (2002).

[6] I. Galanakis, P. H. Dederichs, and N. Papanikolaou, Phys. Rev. B **66**, 174429 (2002).

[7] H. C. Kandpal, C. Felser, and R. Seshadri, J. Phys. D: Appl. Phys. **39**, 776 (2006).

[8] I. Galanakis, P. Mavropoulos, and P. H. Dederichs, J. Phys. D: Appl. Phys. **39**, 765 (2006).

[9] I. Galanakis, J. Phys.: Condens. Matter **16**, 3089 (2004).

[10] S. Skaftouros, K. Özdoğan, E. Şaşıoğlu, and I. Galanakis, Phys. Rev. B **87**, 024420 (2013).

[11] W. H. Butler, A. W. Ghosh *et al.*, see http://heusleralloys.mint.ua.edu/ for "Heuslers Home" (2016).

[12] G. Kresse and J. Furthmüller, Comput. Mater. Sci. **6**, 15 (1996).

[13] P. E. Blöchl, O. Jepsen, and O. K. Andersen, Phys. Rev. B **49**, 16223 (1994).

[14] J. P. Perdew, K. Burke, and M. Ernzerhof, Phys. Rev. Lett. **77**, 3865 (1996).

[15] K. Buschow, P. van Engen, and R. Jongebreur, J. Magn. Magn. Mater. **38**, 1 (1983).

[16] B. Pradines, L. Calmels, and R. Arras, Phys. Rev. Appl. **15**, 034009 (2021).

[17] B. Hülsen, M. Scheffler, and P. Kratzer, Phys. Rev. Lett. **103**, 046802 (2009).

[18] K. Munira, J. Romero, and W. H. Butler, J. Appl. Phys. **115**, 17B731 (2014).

[19] M. Sicot, P. Turban, S. Andrieu, A. Tagliaferri, C. D. Nadai, N. Brookes, F. Bertran, and F. Fortuna, J. Magn. Magn. Mater. **303**, 54 (2006).

[20] P. Turban, S. Andrieu, B. Kierren, E. Snoeck, C. Teodorescu, and A. Traverse, Phys. Rev. B **65**, 134417 (2002).

[21] P. Turban, S. Andrieu, E. Snoeck, B. Kierren, and C. Teodorescu, J. Magn. Magn. Mater. **240**, 427 (2002).

[22] A. R. Rocha, V. M. García-Suárez, S. Bailey, C. Lambert, J. Ferrer, and S. Sanvito, Phys. Rev. B **73**, 085414 (2006).

[23] J. Soler, E. Artacho, J. Gale, A. García, J. Junquera, P. Ordejón, and D. Sanchez-Portal, J. Phys.: Condens. Matter **14**, 2745 (2002).

[24] J. M. Soler, E. Artacho, J. D. Gale, A. García, J. Junquera, P. Ordejón, and D. Sánchez-Portal, J. Phys.: Condens. Matter **14**, 2745 (2002).

[25] S. Huzinaga, Comput. Phys. Rep. **2**, 281 (1985).

[26] R. Poirier, R. Kari, and I. G. Csizmadia, *Handbook of Gaussian Basis Sets* (Netherlands, Elsevier, 1985).

[27] J. Junquera, O. Paz, D. Sánchez-Portal, and E. Artacho, Phys. Rev. B **64**, 235111 (2001).

[28] S. Datta, *Quantum Transport: Atom to Transistor* (Cambridge University Press, 2005).

[29] A. Ghosh, *Nanoelectronics—A Molecular View* (World Scientific, 2016).

[30] Y. Xie, I. Rungger, K. Munira, M. Stamenova, S. Sanvito, and A. W. Ghosh, *Nanomagnetic and Spintronic Devices for Energy-Efficient Memory and Computing* (John Wiley & Sons, Ltd, 2016), Vol. 91.

[31] W. H. Butler, Sci. Technol. Adv. Mater. **9**(1), 014106 (2008).

[32] A. MacDonald, T. Jungwirth, and M. Kasner, Phys. Rev. Lett. **81**, 705 (1998).

[33] P. Damle, A. Ghosh, and S. Datta, Chem. Phys. **281**, 171 (2002).